



HAL
open science

Plasmon Active Functional Coatings with Hybrid Bimetallic Nanoparticles@Polymers by a Single Step Photoinduced Approach

Joachim Haemers, Didier Zanghi, Emmanuel Le Bec, Cécile Genevois, Samar Hajjar-Garreau, Lavinia Balan

► **To cite this version:**

Joachim Haemers, Didier Zanghi, Emmanuel Le Bec, Cécile Genevois, Samar Hajjar-Garreau, et al.. Plasmon Active Functional Coatings with Hybrid Bimetallic Nanoparticles@Polymers by a Single Step Photoinduced Approach. ACS Applied Optical Materials, 2024, 2 (1), pp.199-210. 10.1021/ac-saom.3c00394 . hal-04665612

HAL Id: hal-04665612

<https://hal.science/hal-04665612v1>

Submitted on 31 Jul 2024

HAL is a multi-disciplinary open access archive for the deposit and dissemination of scientific research documents, whether they are published or not. The documents may come from teaching and research institutions in France or abroad, or from public or private research centers.

L'archive ouverte pluridisciplinaire **HAL**, est destinée au dépôt et à la diffusion de documents scientifiques de niveau recherche, publiés ou non, émanant des établissements d'enseignement et de recherche français ou étrangers, des laboratoires publics ou privés.

Plasmon active functional coatings with hybrid bimetallic nanoparticles@polymers by a single step photoinduced approach

*Joachim Haemers,^a Didier Zanghi,^a Emmanuel Le Bec,^a Cécile Genevois,^a Samar Hajjar-
Garreau,^b Lavinia Balan^{a*}*

^a Université d'Orléans, CNRS UPR 3079, Conditions Extrêmes Matériaux Haute Température et Irradiation (CEMHTI), Orléans, France

^b Institut de Science des Matériaux de Mulhouse (IS2M), 15 rue Jean Starcky, MULHOUSE, France

*Corresponding author: lavinia.balan@cnrs-orleans.fr

Abstract:

This study presents a direct method for creating bimetallic nanoparticles (Ag/Au BNPs) within a polymerizable host by a UV light process under atmospheric conditions (air, temperature and pressure). This approach offers both simplicity and efficiency by combining the photo-induced reduction of metal precursors (AgNO₃ and KAuCl₄) and the radical photopolymerisation of a polyethylene glycol diacrylate in a single step. As a result, plasmon active coatings were obtained with three different BNPs in the form of Ag-Au alloy or core-shells (Ag@Au or

Au@Ag) confined in the polymer matrix, with an average diameter between 4 and 6 nm respectively. The method requires only 15 to 45 minutes depending on the desired BNPs system that were easily triggered by playing with the redox potentials of the metal pairs and small amounts (200-300 μ L) of water or acetonitrile solvents used to dissolve these precursors. This control determines which metal is reduced first to form the core and which follows for the shell, or even both simultaneously for the formation of the alloy system. Moreover, double-layered systems such as Ag@Au@Ag can also be synthesised with this approach. Various advanced characterisation techniques, including real-time UV-Vis spectroscopy, X-ray photoelectron spectroscopy, X-ray absorption spectroscopy, and transmission electron microscopy (in particular STEM-HAADF imaging and EDS elemental mapping), were used to monitor the synthesis process and identify the formed BNPs system.

These new plasmonic materials exhibit unique optical properties depending on the BNPs system, making them promising for multiple applications such as sensing, SERS, optics, catalysis or photocatalyse, and easily scalable for large-scale production.

Keywords: bimetallic nanoparticles, plasmon active nanocomposites coating, photo-induced synthesis, photopolymers, hybrid nanomaterials

Introduction:

Noble metal nanoparticles (NPs), i.e. silver, gold or platinum, are sought after for their attractive optical properties, which can be used in wide variety of fields such as biomedicine [1, 2, 3, 4], catalysis [5, 6, 7, 8], photovoltaics [9, 10] or sensing [11, 12, 13, 14] especially SERS (Surface-enhanced Raman spectroscopy) applications [15, 16]. In particular, the localised surface plasmon resonance (LSPR), which is specific to each noble metal, provides insight into the shape and size distribution of NPs.

Moreover, the combination of two noble metals to form bimetallic nanoparticles (BNPs) offers a wider range of properties that can be tuned as a function of the choice and proportion of each metal [17]. For example, the combination of silver and gold improves the overall photocatalytic properties by increasing the electronic density on the surface of the NPs [6, 18], and the addition of gold to silver can improve the stability or resistance to oxidation of silver NPs [19].

In solution, these BNPs are typically synthesised as alloys or core-shell structures using various techniques [20], which can be either top-down or bottom-up processes. In this second approach, BNPs in solution can be synthesised by chemical reduction reactions, which are often developed to obtain nano-alloys by adding reducing agents, such as citrate [21, 22], NaBH_4 [23], hydrazine [24, 25] or plant extracts [1, 7, 8, 26], to metallic precursors. The issue with colloidal NPs is their tendency to aggregate in the absence of surface stabilisers, which have been shown to increase their stability, but only to a certain extent [23]. In addition, the chosen solvents and/or stabiliser molecules may be toxic, limiting the potential applications. To avoid these problems, and because the majority of daily life applications of NPs are needed in solid matrixes or coatings, BNPs are directly synthesised on or within various solid matrixes, especially polymers for functional surfaces. For example, Ghodselahi et al. [27] obtained nanoalloys by

radiofrequency sputtering on glass, although this technique requires the use of acetylene gas in a vacuum medium of ~ 2 Pa. Electrodeposition was used by Dong et al [14] to synthesise core-shell BNPs on indium tin oxide via a two-step deposition method, for the core and shell, respectively. In polymers, alloy BNPs have been created on flexible polyarylene ether nitrile, by using a high vacuum ($\sim 10^{-4}$ Pa) and an annealing step between 250 and 310 °C [28] or in polyethylene glycol by double target sputtering [29], also requiring the use of an ultrahigh vacuum and long thiol molecules to protect the obtained nano-objects. More recently, vapour-induced phase separation allowed the formation of bimetallic hetero-oligomers in a poly(methyl methacrylate) (PMMA) nanoholes matrix [30]. This technique involves the formation of PMMA layers by multiple steps of spin coating and solvent evaporation in which the BNPs were formed after 7 days of silicon (N-doped) induced reduction [30]. In addition, chemical reduction methods have also been used to synthesise alloyed BNPs within a polymer matrix, such as cellulose, using NaBH_4 in the presence of sodium citrate to control the size of the NPs [31]. Moreover, the polymer itself, namely cellulose, polyethylene glycol (PEG), or chitosan, can act as both matrix and reducing agent [6, 18, 32]. However, these methods require the polymer to be dissolved in NaOH with additional steps. In the case of cellulose, several steps are followed by heating at 80°C for a total of 70 min [6], while for PEG, heating between 140 and 180 °C was required to boil the mixture of PEG and NaOH dissolved in water [18].

To avoid the use of harmful products or processes, a photoinduced approach has been developed to synthesise monometallic NPs in a photopolymerisable matrix by combining the photoinduced synthesis of metal NPs and the photocrosslinking of monomers [33, 34, 35, 36].

In the present work, this photoinduced approach was extended to create BNPs (silver and gold) in an efficient and one-step process under atmospheric conditions (air, temperature and pressure).

The photopolymerisable matrix effectively confined and stabilised the BNPs due to the rapid crosslinking process, resulting in plasmonic active coatings. In addition, different types of hybrid BNPs@polymers nanocomposites were obtained by modifying the chemical parameters of the reactions to control the reduction order of the metal precursors. This offers versatility and allows the creation of BNPs including Ag-Au alloys and core-shell structures (Ag@Au or Au@Ag).

However, as will be highlighted in what follows, the complexity of the systems used makes any form of predictive analysis with quantitative aims rather illusory. Indeed, the formulation in which the oxido-reductive processes involved take place, consists mainly of a diacrylate monomer. It exhibits an initial viscosity of around 100 mPa.s at 25°C, which increases as the conversion progresses. As a result, diffusional processes are increasingly slowed down. Finally, it is important to bear in mind that the primary radicals resulting from photolysis of the photoinitiator are involved in two processes: the initiation of crosslinking polymerization and the reduction of Ag(I) and Au(III) species. The balance between these competing processes is defined by both thermodynamic and kinetic considerations, the latter evolving over time as a function of the polymerization rate.

Nevertheless, in an attempt to identify the parameters that determine and the order of Ag(I) and Au(III) reductions, i.e., which ones will lead to the core and shell formation respectively, the reactions were followed by UV-visible, X-ray photoelectron (XPS) and X-ray absorption spectroscopies (XAS), as well as transmission electron microscopy (TEM) as a function of UV exposure time.

Materials and methods:

Reagents:

Silver nitrate, AgNO₃, (“cryst. extra pure” from Merck) was used as a silver precursor after grinding by with a pestle and mortar. Potassium tetrachloroaurate (III), KAuCl₄, (99.995% trace metals basis) 2-hydroxy-2-methylpropiophenone, used as photoinitiator (PI) (97%) and ammonium hydroxide solution (28.0-30.0%) from Sigma Aldrich, were used as received. Acetonitrile (AcN), (≥ 99.5 %) from Carl Roth and Polyethylene Glycol (600) Diacrylate (PEGDA) presenting a viscosity of 100 mPa.s at 25°C, from Sartomer Arkema were used as received.

Instrumentation:

The UV source used for the BNPs@polymers nanocomposites’ synthesis was a Hamamatsu Lightningcure LC8 (Hg-Xe L8252) with a fluence of 450 mW.cm⁻² in the 250-445 nm range. UV-visible absorption spectrophotometer Evolution 220 from Thermo Scientific was used to monitor BNP synthesis and growth via the LSPR. The spectra obtained were then fitted with one or two Lorentzian line profiles, to determine the values of the centre of each contribution (an example is shown in Figure S1 along with a description of the method used).

High Resolution Transmission Electron Microscopy (HRTEM), Scanning Transmission Electron Microscopy High Angle Annular Dark Field (STEM-HAADF) imaging, Energy-dispersive X-ray spectroscopy (EDS) and elemental mapping were performed on a JEOL ARM200F (JEOL Ltd.) Cold Field Emission Gun TEM operating at 200 kV, equipped with a double-spherical aberration (Cs) correctors and fitted with a JOEL SDD CENTURIO EDS system. The STEM-HAADF images were acquired with an inner-outer collection angles of 68-174.5 mrad and a 0.1 nm probe size. For the imaging, the hybrid nanocomposite films were

ground, dispersed in ethanol prior to analysis and a droplet of this low concentration mixture was placed on a copper TEM grid.

X-ray absorption spectroscopy (XAS) was carried out on the SAMBA beamline at the SOLEIL synchrotron facility. Measurements were performed at the K edge for Ag (25.514 keV) and the L3 edge for Au (11.919 keV) at room temperature in the X-ray fluorescence mode on polymer films deposited on a glass substrate at an angle of 45°. The detector used was a 36-element planar monolithic Ge pixel array (Camberra) equipped with Soller slits and X-ray filters (Pd and Ge for the Ag and Au edges respectively). The detector was placed 90 mm from the sample to obtain a dead time of 10-20% and a number of detected X-ray photons of 20,000-30,000 counts/s. For each sample, X-ray absorption spectroscopy (XAS) was performed at the K-Ag and L3-Au thresholds. The EXAFS signal was extracted using Athena software based on the IFEFFIT library of analytical and numerical algorithms [37]. The structural parameters N and R (N, the number of first neighbours; R, the distance between the absorbing atom and its first neighbours) were obtained from the simulation of the EXAFS oscillations using Artemis software. The procedure used for this fit is described in SI. An example of a fit performed simultaneously on data recorded for both thresholds on the same sample is also shown in SI. Using the structural model of Hwang et al. [38] (see in the SI) based on the coordination number of silver and gold atoms, it was inferred, the random distribution of Ag and Au metal atoms within a bimetallic nanoparticle to identify the type of BNP formed after different UV exposure times.

X-ray Photoelectron Spectrometry (XPS) was performed on a VG Scienta (Upsalla) SES 200-2 spectrometer under ultra-high vacuum to identify the different phases in the hybrid coating. The XPS measurements were carried out using photons from a monochromatized Al K α source

(1486.6 eV). The spectra were recorded using a pass energy of 500 eV for wide scans and 100 eV for high resolution.

Results and discussion:

Photoinduced synthesis of bimetallic nanoparticles in a photopolymer matrix:

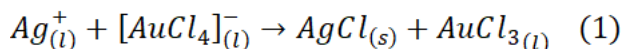
Three photosensitive formulations (Table 1) have been proposed to obtain the different hybrid BNPs@polymers coatings. They are based on a mixture of PEGDA acrylate monomers with 0.8 wt. % of PI, used as free radical generators and AgNO₃ and KAuCl₄ as metal precursors. In all three cases, the concentration of both metal precursors was 0.5 wt. % corresponding to an atomic ratio of 2.2:1. The liquid mixture was then deposited onto microscope glass slides before being passed through a bar coater to produce a 100 μm thick film and consequently exposed to a UV lamp for several minutes.

Table 1. Synthesis conditions of the three photosensitive formulations: Ag@Au, Ag-Au and Au@Ag.

| Formulation 1: Ag@Au | Formulation 2: Ag-Au | Formulation 3: Au@Ag |
|--|---|--|
| At. ratio Ag: Au 2.2:1 0.5 wt. % AgNO ₃ and 0.5 wt. % KAuCl ₄ | | |
| <ul style="list-style-type: none"> - Dissolution of AgNO₃ in H₂O (125 μL) with NH_{3(aq)} (25 μL), stirred 15 min - Dissolution of KAuCl₄ in H₂O (125 μL) - Addition of dissolved gold into the silver solution, stirred 15 min - Addition of the mixture PEGDA/PI, stirred 1 hour | <ul style="list-style-type: none"> - Dissolution of AgNO₃ in H₂O (125 μL) - Addition of the mixture PEGDA/PI to the silver solution, stirred 15 min - Dissolution of KAuCl₄ in H₂O (125 μL) - Addition of dissolved gold into the silver/monomer solution, stirred 1 hour | <ul style="list-style-type: none"> - Dissolution of KAuCl₄ in AcN (200 μL) - Addition of AgNO₃ - Addition of AcN (300 μL), stirred 15 min - Addition of the mixture PEGDA/PI, stirred 1 hour |

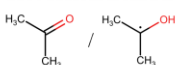
These formulations were designed to control the order of the photo-induced reduction of the metal precursors and were based on several points.

Firstly, the spontaneous formation of AgCl, a solid precipitate, when the two metal precursors are brought into contact [39] (*Eq. 1*). This compound has a low solubility (solubility constant $1.77 \cdot 10^{-10}$ [40]), and it is expected to react more slowly than $\text{Ag}^+_{(l)}$ and $[\text{AuCl}_4]^-_{(l)}$.



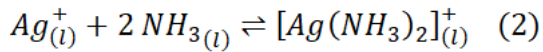
Secondly, the oxidation/reduction potentials, E^0 are shown in Table 2. However, these thermodynamic values do not give any information about the kinetics of the reactions. Indeed, the formulation in which the oxido-reductive processes take place consists mainly of an acrylate monomer with a viscosity of 100 mPa.s at 25°C.

Table 2. Redox potentials of the metal precursors, different compounds formed in the reactions and free radical formed by PI [41, 42, 43].

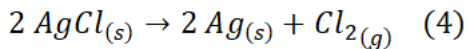
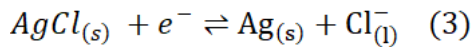
| Red/Ox couple | E^0 (V) |
|--|-------------|
| Au^{3+}/Au | 1.50 [41] |
| $[\text{AuCl}_4]^- / \text{Au}$ | 1.00 [41] |
| Ag^+ / Ag | 0.80 [41] |
| $[\text{Ag}(\text{NH}_3)_2]^+ / \text{Ag}$ | 0.38 [42] |
| AgCl / Ag | 0.22 [41] |
| Free radical from PI:  | - 0.83 [43] |

Thirdly, UV-visible spectroscopy measurements on the synthesis of monometallic particles show that the photo-induced reduction of gold precursor (KAuCl_4) is 10 times longer than that of the silver one (AgNO_3) under identical conditions (Figure S4). Indeed, the Au^{3+} to $\text{Au}(0)$ reduction is more complex and consists in, at least three elementary steps of which one is bimolecular, explaining the slower kinetics.

With this in mind, for the first formulation (Ag@Au), and in order to partially neutralise the formation of AgCl when Ag^+ reacts with the $[\text{AuCl}_4]^-$ complexes (Eq. 1), a small amount of $\text{NH}_3(l)$ (25 μL) was added to the AgNO_3 solution, The resulting ammine complexes $[\text{Ag}(\text{NH}_3)_2]^+$ (Eq. 2) [44, 45] show increased reactivity with respect to AgCl. This complex can then be reduced into Ag(0) more favourably than $\text{AgCl}_{(s)}$ (Table 2). In addition, silver in this complex form, will be reduced before $[\text{AuCl}_4]^-$. As the reaction is exothermic, the amount of ammonia is deliberately limited, so that the heat generated does not trigger the polymerisation of the PEGDA monomers introduced into the formulation.

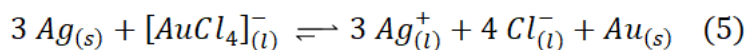


For the second formulation (Ag-Au), the same protocol was followed, this time favouring the formation of AgCl by not adding ammonia to the initial aqueous AgNO_3 solution. The formation of this intermediate solid compound slows the production of Ag(0) (Eq. 3), which awaits the reduction of the $[\text{AuCl}_4]^-$ complexes. However, this precipitate is light sensitive and can cause the formation of Ag(0) (Eq. 4). The addition of extra silver atoms due to the partial reduction of AgCl will then favour the reduction of gold precursors, mixing silver and gold particles which grow to form an alloy. The remaining AgCl can then be reduced along with the gold as the reaction continues.



For the third formulation (Au@Ag), the idea was to reduce the gold precursor before the silver precursor and to have gold as the core and silver as the shell. To achieve this, the order in which the solutions were mixed was reversed and water was replaced with acetonitrile, a solvent of

lower polarity. The aim here is to allow time for the $[AuCl_4]^-$ complexes to be first reduced to Au(0) by slowing the reduction of AgCl to Ag(0). In addition, the presence of silver seeds accelerates the reduction of gold while delaying the reduction of silver (*Eq. 5*) [3, 46]. Once the gold precursor has been reduced, AgCl can then be reduced.



In situ monitoring of BNPs formation and growth by UV-Vis spectroscopy:

The photoinduced synthesis of BNPs@polymer hybrid nanocomposites for these three formulations was monitored by *in situ* UV-Vis spectroscopy in order to observe the different stages of BNPs formation (

Figure 1) as a function of the exposure time to UV light. The aim is to verify the hypothesis about the oxidation-reduction reactions that allow the growth of the three types of bimetallic particles considered during the preparation of the formulations.

Firstly, it should be noted that for all three systems, no absorbance peaks were observed in the visible light wavelength range, which could be associated with the presence of metallic silver or gold particles at the beginning of the exposure time (0 s).

Subsequently, whatever the formulation, the absorbance spectra obtained over the exposure time to UV light all show one surface plasmon resonance (LSPR) peak, rather than two well-separated peaks that could correspond to the signals of silver (404 nm) and gold (541 nm) monometallic particles (experimental values taken from Figure S4), as observed for films consisting of a mixture of silver and gold monometallic nanoparticles [3, 47, 48, 49].

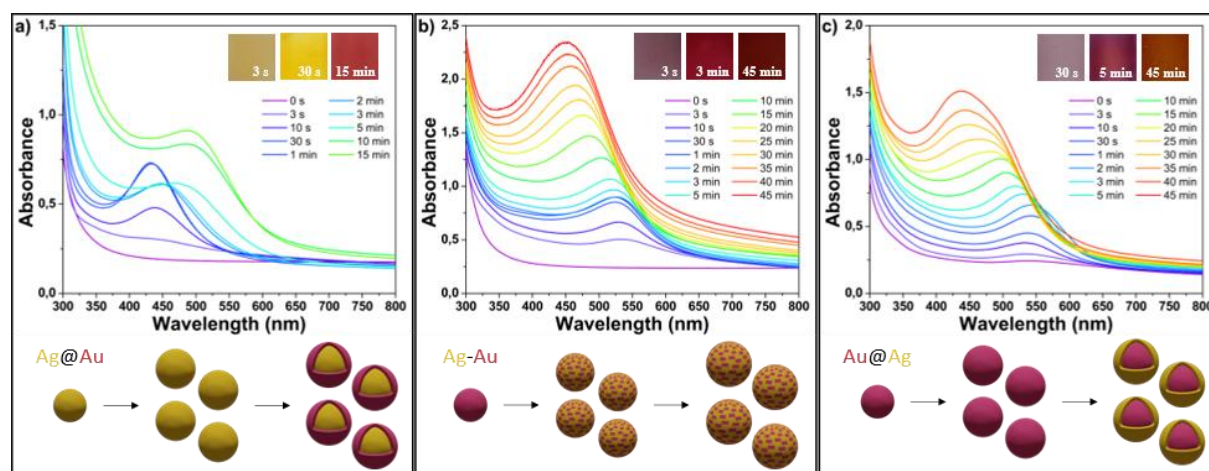


Figure 1. *In situ* UV-Vis absorption spectra of BNPs as a function of the UV exposure time: a) Ag@Au NPs b) Ag-Au NPs and c) Au@Ag NPs. Inserts: Pictures of the coatings on glass at 3s, 30s and 15 mins for the Ag@Au NPs; at 3s, 3 mins and 45 mins for the Ag-Au alloy NPs; at 30s, 3 mins and 45 mins for Au@Ag NPs and schematic representation of the BNPs growth according to LSPR.

The *in-situ* monitoring of the first formulation (Ag@Au) under light-exposure (

Figure 1a) started with the appearance of a peak at 452 nm after 3s and a yellow colouring of the coating (see insets

Figure 1a), related to the formation of silver NPs. After 30s, the peak began to slowly shift to the red, losing intensity up to 3 mins, and after which it regained intensity with a peak at 506 nm after 5 min. These effects could be the beginning of gold formation around silver, explained by the gradual masking of the silver LSPR by the gold one. It has been noted that in core-shell hybrids the LSPR is dominated by that of the shell [50]. In addition, gold continued to grow with a clear peak at 523 nm after 10 mins and reached 515 nm after 15 mins of exposure. The growth

of nano-sized Au(0) was also visible by the colour change of the coating from yellow to pink (see insets

Figure 1a).

In the second formulation (Ag-Au), (

Figure 1b), the reduction of the precursors starts very quickly (3s) with a LSPR at 535 nm, indicating the presence of AuNPs that continuously shifts to lower wavelengths until 457 nm. At the same time, the colour of the solid coating changes from dark purple to dark orange (see insets

Figure 1b). At the end of the exposure, after 45 mins, only a broad peak was observed, which could be characteristic of $\text{Ag}_x\text{Au}_{1-x}$ alloys, as shown by Eremenko et al. and Gonzalez et al. for alloy BNPs obtained in solution and stabilised by surfactants [47, 48, 51].

Monitoring of the third formulation (Au@Ag), (

Figure 1c) initially shows a clear LSPR at 543 nm at 10s exposure time and a purple colour of the coating confirming the formation of AuNPs. After 3 mins of exposure, the LSPR increases and starts to shift towards the blue, which could be the starting point of the Ag(0) formation. After 30 mins, the growth of a second peak at 432 nm was clearly observed, which increased in intensity and shifted towards the blue with the increasing exposure time, ending at 424 nm after 45 mins of UV-exposure. This can be correlated to the increasing thickness of the silver layer. The colour of the coating also changed from purple to orange during the reaction, confirming the transition from gold to silver. In the final spectra at 45 mins, the contribution of the Ag(0) at 424 nm is more intense than that of the Au(0), which could be characteristic of a Au@Ag core-shell system [47, 48, 51, 52]. The evolution of these spectra is similar to that of Ag@Au, although reversed. Here, the silver shell dominates the LSPR of the Au(0) core.

Structural characterisation of obtained photoinduced BNPs:

The *in-situ* monitoring of BNP growth using UV-Vis spectroscopy confirmed the hypotheses made about the chemical syntheses that led three different types of bimetallic particles depending on the prepared formulations. However, further investigations were carried out using different techniques, namely TEM, XPS and EXAFS, in order to give more substance to these observations.

TEM micrographs showed that the NPs were well dispersed in the polymer matrix, with spherical shapes for the three systems (Figure 2). Statistical size analysis of 100 particles shows average diameters of 4.4, 4.2 and 5.9 nm for Ag@Au, Ag-Au and Au@Ag respectively (insets Figure 2). For the Ag@Au and Au@Ag systems, the difference in contrast observed between the core of the particles (darker) and the periphery (lighter grey) when zooming in on the micrographs, also seems to be consistent with the formation of core-shell structures (Figure 2 a and c). No clear contrast was observed for the Au-Ag system (Figure 2 b), which could indicate a BNP alloy structure. Additional HRTEM and STEM-HAADF imaging can be found in the supplementary information Figure S5.

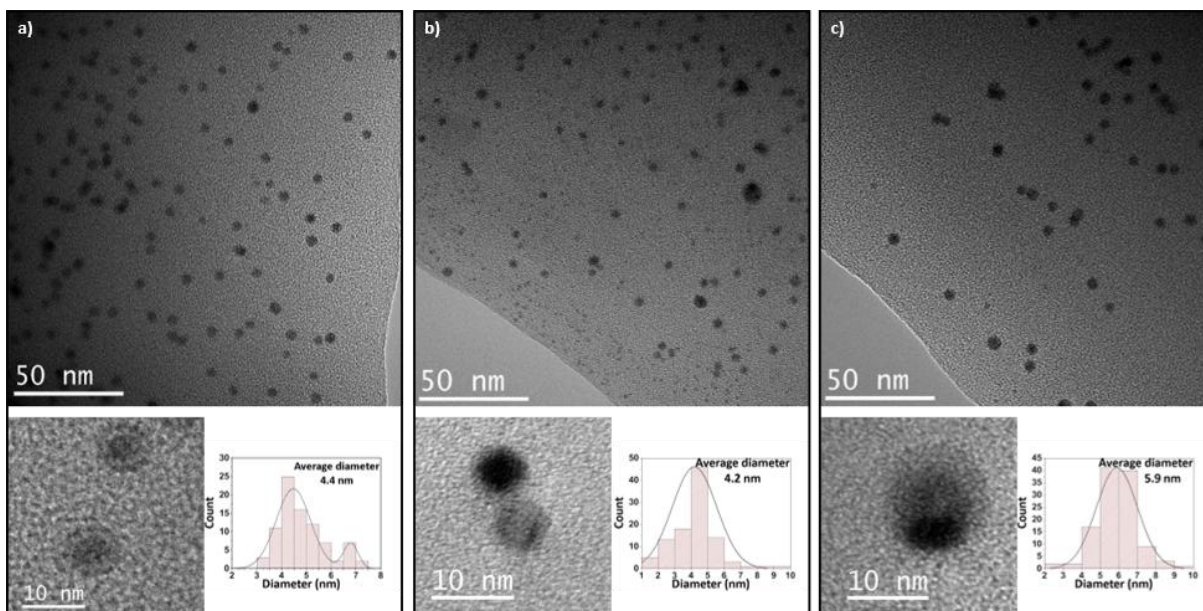


Figure 2. TEM micrographs of the BNPs in the polymer matrix: a) Ag@Au after 15 min UV exposure, b) Ag-Au after 45 min UV exposure and c) Au@Ag after 45 min UV exposure with a zoom on one or two BNPs and the sizes distribution histograms of the NPs.

In the case of the first system, Ag@Au, a kinetic study of BNP formation was carried out using different exposure times by X-ray absorption spectroscopy (XAS) and TEM combined with elemental mapping by EDS and STEM HAADF imaging. The exposure times were chosen to correspond to the transition from one LSPR peak to another as measured by UV-visible spectroscopy (

Figure 1): 30 s for Ag formation (0) and 15 min for Au formation (0).

Analysis of TEM images taken at different kinetic stages of the photo-induced oxidation-reduction reactions for the Ag@Au system (Figure 3a) revealed the presence of spherical NPs whose mean diameter increased with increasing exposure time. The change from a diameter of 3.1 nm after 30 s to 4.4 nm after 15 min (Figure 3) could mean that the gold shell formed around the silver core has a thickness of 1.6 nm (Figure 3a).

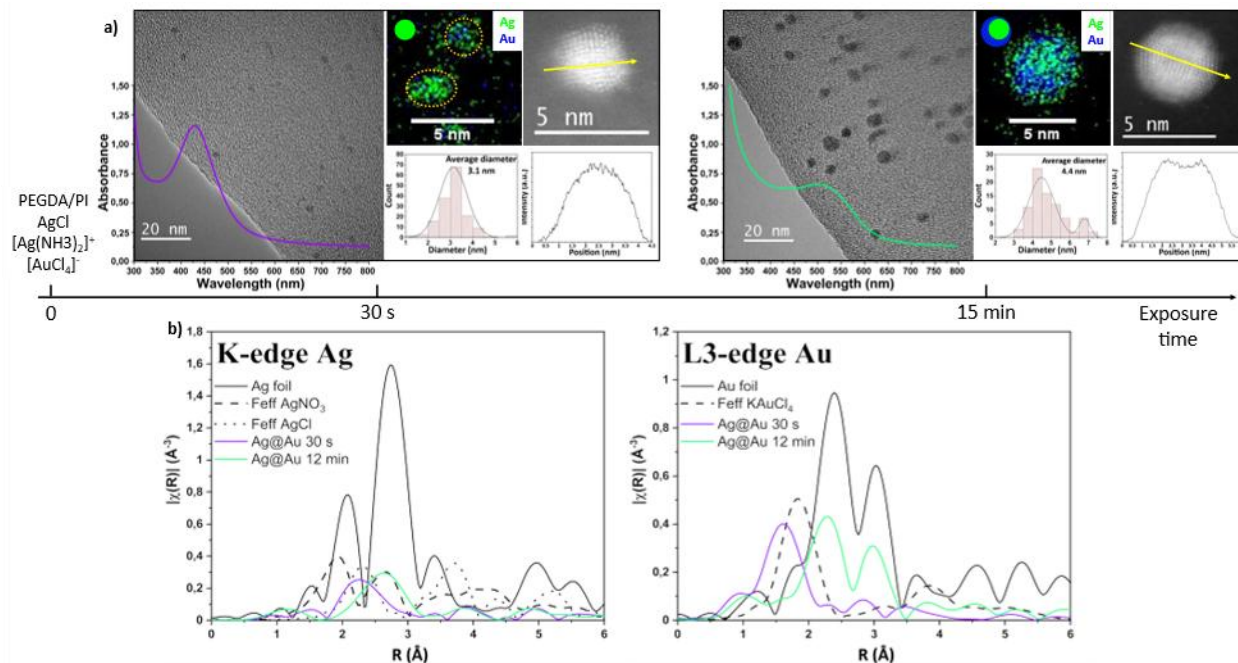


Figure 3. Ag@Au system: a) At 30 (left)s and 15 mins (right), TEM micrographs with the elemental mapping (Ag green and Au blue) and size histograms in inserts and STEM HAADF imaging and the corresponding intensity profile b) the EXAFS data for the K-edge Ag on the left and the L3-edge Au on the right with UV-Vis Kinetic spectra of the growth of Ag@Au NPs for three different exposure time: 0s (black), 30s (purple) and 15mins (green).

For the sample exposed to UVs for 30 s, EDS mapping shows the very clear formation of a majority of silver NPs (Figure 3a left), which is confirmed by the bell-shaped intensity profile drawn across a grain on the STEM-HAADF image, indicating the presence of monometallic particles [53]. In STEM-HAADF (Z-contrast) imaging mode, the intensity is directly proportional to the thickness and the composition of the sample. The heavier the element or thicker the sample, the clearer it appears. These results are consistent with the Ag(0) LSPR peak observed in the UV-Vis absorption spectrum at 30s (Figure 3 UV-Vis spectra). EDS mapping of the grain (inset Figure 3a on the left) shows that very few gold NPs have yet appeared.

The Fourier transforms of the EXAFS oscillations (Figure 3b, purple curves left and centre) recorded at the K-Ag and L3-Au thresholds for this 30 s sample were very different from those obtained for the reference silver and gold foils. This difference suggests that the metals are not completely reduced, and that the oxidation-reduction reaction is not fully completed for this formulation. To confirm this hypothesis, the EXAFS signals Fourier transforms of the AgCl, AgNO₃ and KAuCl₄ compounds, simulated with the Feff calculation code [54], were compared that of the experimental EXAFS signal of the Ag@Au sample (30s). At the silver K-edge, the experimental signal is similar to that of the AgCl compound (Figure 3b, dashed black curve). The fact that the first peak of the Fourier transform is not completely symmetrical probably indicates the existence of an additional contribution due to the significant presence of Ag(0), as suggested by the absorption peak detected by UV-visible spectroscopy. With regard to the gold signal, the experimental signal recorded at the L3 gold edge is very close to that simulated for a KAuCl₄ precursor salt identical to that used in the formulation. This supports the idea that the gold was not yet reduced at this stage of the reaction.

After 15 mins of UV exposure, both metals are visible on the EDS map (Figure 3a right). The AgNPs appear more concentrated in the centre of the NPs, while a mixture of gold and silver was observed at the periphery. The intensity profile plotted along the grain diameter (see Figure 3a right), in the STEM-HAADF image, actually shows a decrease in intensity in the centre of the particles, indicating the presence of silver and gold on the outside. This profile is identical to that simulated by Li et al [53] on Ag@Au core-shells. Thus, after 15 mins, the BNPs therefore have a silver-rich core and a gold-rich shell. The EXAFS measurements carried out on the samples subjected to this exposure time (Figure 3b, green curves) show that gold was completely reduced and silver only partially. The Fourier transform of the EXAFS signal at the L3 threshold for gold

is indeed comparable to that of the gold foil. Compared to the 30s sample, the first peak of the Fourier transform at the Ag K-edge has been shifted to the right and is superimposed on the second peak of the Fourier transform of the AgNO₃ signal. This peak is also very close to the position of the second peak of the silver foil at the silver K-edge. The absence of a first peak on the Fourier transform around 2 Å, characteristic of the presence of Ag(0), is probably due to the fact that this is a mixture of AgNO₃ and residual AgCl as well as a small amount of Ag(0), which produces a single relatively broad peak of low intensity. Simulations of EXAFS oscillations at the silver K and gold L3 thresholds give a very low coordination number for silver ($N_{\text{Ag-Ag}} = 2.4 \pm 0.4$) and a very high one for gold ($N_{\text{Au-Au}} = 12.0 \pm 2.2$). This value is comparable to that of a solid gold sample, indicating that the Au(0) layer is very thick compared to the Ag(0) one.

Since silver is not completely reduced within 15 min in the given formulation, it is difficult to estimate the precise amounts of Ag(0) and Au(0) present in the samples. This challenge hindered the ability to calculate the J parameters required for Hwang's structural model [38] which could have identified the nature of the bimetallic particles formed and allow further analysis of the data obtained from the EXAFS measurements.

For the other two systems studied (Ag-Au and Au@Ag), XAS measurements were performed on samples exposed for times, 30 s and 45 mins for the Ag-Au system and 2 mins and 45 mins for the Au@Ag system (Figure 4). These times were chosen because they correspond to the LSPR peak transition from silver to gold and vice versa on the UV-Vis spectroscopy curves (

Figure 1).

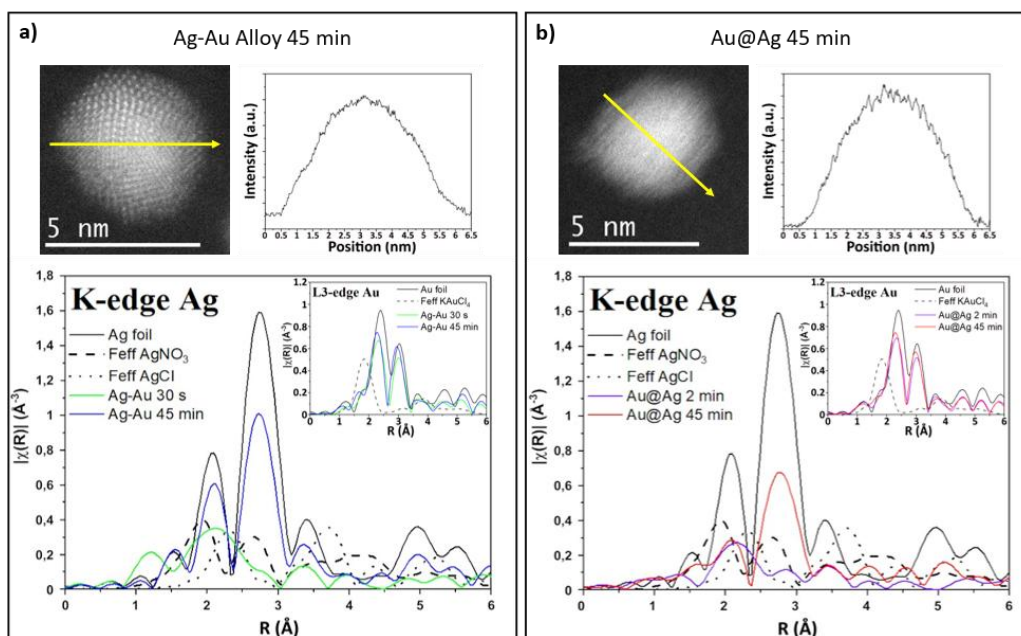


Figure 4. Comparison of the a) Ag-Au alloy and the b) Au@Ag BNPs through STEM-HAADF imaging, EXAFS data on the silver K-edge (and gold L3-edge in insert).

For short exposure times, in both cases (Ag-Au and Au@Ag) it was found that the Fourier transforms of the EXAFS oscillations recorded on the L3-Au are very close to those observed for bulk gold. In contrast to the Ag@Au system, gold was reduced very rapidly in these formulations, as shown by the UV-visible spectra (

Figure 1). On the other hand, the signals obtained at the K-Ag indicate little to no silver in these formulations and that it is essentially present in the form of a mixture of AgNO₃ and AgCl. However, in the case of the Ag-Au system, the width of the first peak of the Fourier transform and the appearance of a small shoulder at about 2.8 Å could indicate the existence of a third contribution due to the presence of Ag(0). Considering the low amplitude of the signal and the absence of a pure Ag(0) phase, the EXAFS signals were not simulated.

For Au@Ag and Ag-Au samples exposed to UV for 45 mins, the Fourier transforms of the EXAFS signals measured at the silver and gold thresholds are identical to those obtained for solid silver and gold samples. The metal precursor salts have been completely reduced. The decrease in peak amplitude indicates the formation of small clusters of a few nanometres in diameter. In order to determine the number of first neighbors around the gold and silver atoms, the experimental EXAFS oscillations recorded at the K-Ag and the L3-Au thresholds were fitted simultaneously to the theoretical standard EXAFS formula for these two samples (Table 3).

Following the example of Godfrey et al [55] who studied the structure of bimetallic gold and silver colloidal nanoparticles (Au@Ag and Au@Ag@Au) with an average diameter between 27 and 31 nm by XAS, the analysis of the fitted parameters shows a dominant contribution of the monometallic paths (Au-Au and Ag-Ag) at both Au L3 and Ag K-edges. Their results show Au-Au, Ag-Ag coordination numbers of ~ 12 , close to the values obtained for a bulk sample. This indicates that the Au core and Ag shell of the particles are relatively large. In this case, the interactions between the two metals at the core-shell interface had no significant influence, in contrast with the systems studied here (Ag-Au and Au@Ag), for which we obtained Au-Au coordination numbers of 9.8 and 9.0 and Ag-Ag coordination numbers of 6.1 and 6.6 respectively. The fact that the core is smaller and the silver layer thinner in our case means that we also have to consider Au-Ag and Ag-Au diffusion paths in our simulations in order to obtain better fits. However, these contributions are more important ($N_{\text{Au-Ag}} = 2.6$ and 2.3 for the Ag-Au system and $N_{\text{Ag-Au}} = 5.4$ and 1.0 for the Au@Ag system) in our systems which makes the situation more difficult to analyse. To counter this, a structural model proposed by Hwang et al [38] was used to describe the distribution of the two metals in BNPs. This model is based on the coordination numbers $N_{\text{A-A}}$, $N_{\text{B-B}}$, $N_{\text{A-B}}$, $N_{\text{B-A}}$ (A = Ag and B = Au) extracted from the EXAFS

oscillation fit. Moreover, we calculated the J_{Ag} and J_{Au} to compare the data with that obtained for an ideal alloy.

Moreover, for the Ag-Au system, the determination of the coordination numbers of the silver and gold atoms derived from simulations of the EXAFS signals according to Hwang's structural model, gives $J_{\text{Ag}} > 100\%$ and $J_{\text{Au}} < 100\%$, implying that the sample is an alloy with a gold-rich core (Table 3). The simulation in question is shown Figure 5 and was made for two layers of neighbours around the absorbing atom. The intensity profile carried out on the particles observed by STEM-HAADF shows a rounder peak with no small superstructures on either side (Figure 4a).

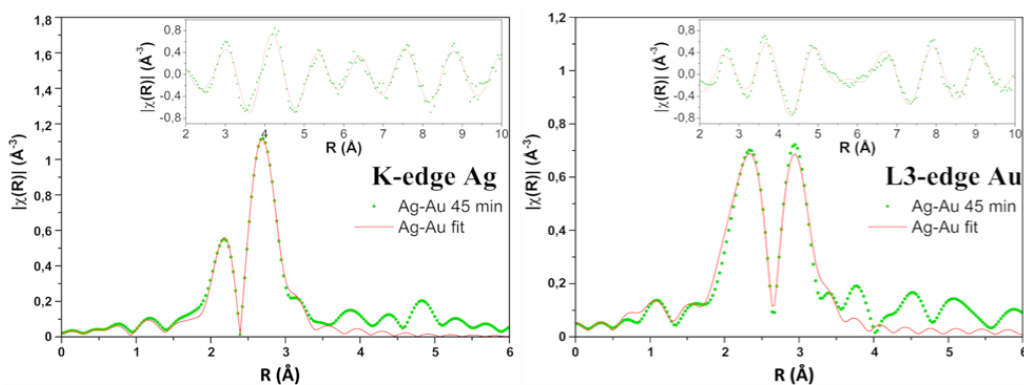
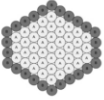


Figure 5. Fits simultaneously made on the K-edge Ag (left) and on the L3-edge Au (right) for Ag-Au after an UV exposure of 45 min.

In the case of the Au@Ag system, the determination of the coordination numbers leads to J parameters both below 50% ($J_{\text{Ag}} < 50\%$ and $J_{\text{Au}} < 50\%$ with $N_{\text{Au-Au}} > N_{\text{Ag-Ag}}$), which according to the structural model used in this work, indicates that the NPs are composed of a gold core and a silver shell (Table 3). The simulation in this case is found in the SI (Figure S2). This seems to be

confirmed by the intensity profile obtained from the STEM-HAADF image (Figure 4b), marked by the presence of two inflection points at 1.5 nm and 4.5 nm, which would be the signature of a core-shell system with a shell lighter than the core, according to simulations carried out by Li *et al.* on an Au@Ag core-shell structure [53].

Table 3. J_{Ag} and J_{Au} structural parameters calculated from the coordination numbers and the structures cases obtained from those calculations. Schemes of the structures are adapted with permission from [38]. Copyright 2005 American Chemical Society

| BNPs | Exposure times | N_{Ag-Ag} | N_{Ag-Au} | N_{Au-Au} | N_{Au-Ag} | J_{Ag} | J_{Au} | Structures | Schemes [38] |
|-------|----------------|---------------|---------------|---------------|---------------|----------|----------|-------------------------|---|
| Ag@Au | 15 min | N/A | N/A | N/A | N/A | N/A | N/A | N/A | N/A |
| Ag-Au | 45 min | 6.1 ± 1.0 | 5.4 ± 2.6 | 9.8 ± 1.2 | 2.6 ± 0.6 | 150 | 30 | Alloy with Au-rich core |  |
| Au@Ag | 45 min | 6.6 ± 1.8 | 1.0 | 9.0 ± 1.0 | 2.3 ± 0.7 | 49 | 29 | Core-shell Au@Ag |  |

To complement these results, X-ray photoelectron spectrometry (XPS) was also carried out on the three systems obtained after a long exposure time of 45 min to UV light (Figure 6a). By analysing the surface of the hybrid polymer film in which the nanoparticles were embedded, it was possible to determine the elements present in the samples by deconvoluting the peaks corresponding to the different electron binding energies of each (Figure 6b, c and d). Moreover, by tilting the sample relative to the analyser it is possible to modify the depth of analysis (Figure 6e). Generally, the electrons are collected along the normal surface, where the emission angle relative to the sample surface is $\theta=90^\circ$ (θ angle between the analyser and the sample surface). In this case, the depth of analysis is around 8 nm. The inclination of the sample increases the angle of emission and the analysis depth is approximately 4 nm (angle $\theta=30^\circ$), see drawings in Figure 6d and e.

For the three systems, only Ag, Au, K, C and O were detected at $\theta=90^\circ$, over an analysed depth of 8 nm (Figure 6a, Figure S6 and S7). For these last two elements, analysis of the line

profile at 286 eV and 532 eV confirms the presence of carbon-oxygen bonds typical of those expected for the PEGDA polymer (Figure 6b and c and Figure S6 and Figure S7).

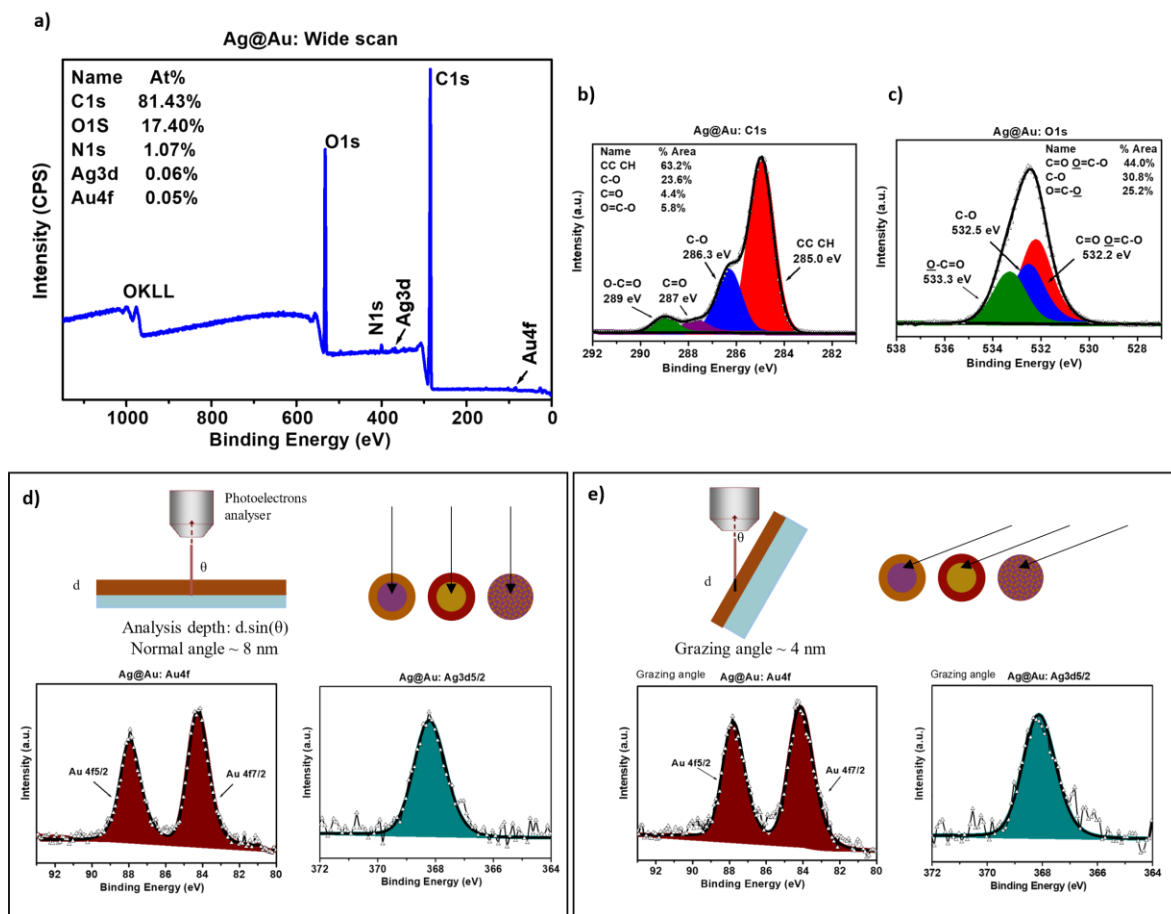


Figure 6. XPS spectra for the Ag@Au: a) wide scan b) deconvolution of the carbon spectra c) deconvolution of the oxygen spectra d) drawing of the probing analysis at a normal angle with the deconvolutions of Au and Ag spectra and e) drawing of the probing analysis at a grazing angle (30°) with the deconvolutions of Au and Ag spectra.

Deconvolution of the Au 4f and Ag 3d core-levels for the Ag@Au system shows no presence of Ag^+ or Au^{3+} ions, which could be related to the presence of chloride or nitrate. Only peaks

corresponding to Ag(0) and Au(0) atoms are detected (Figure 6d). Similar results were observed for the deconvolution of the other two systems, Ag-Au (Figure S6) and Au@Ag (Figure S7).

In order to reduce the probe depth to 4 nm, the emission angle was changed from 90° to 30° relative to the sample surface (see drawings in Figure 6d and e). The atomic percentages of Ag compared to Au are given in Table 4. The atomic percentages were determined using the integrated peak areas of each component, after Shirley background removal and taking into account the cross-section, mean free path of an electron and transmission function of the analyser.

Table 4. Binding energies and relative atomic percentage for Ag 3d from XPS fitting function of the incidence angle.

| Sample | Bond | Detection angle | Binding energy (eV) | At. % |
|--------|----------|-----------------|---------------------|-------|
| Ag@Au | Ag 3d5/2 | Normal | 368.2 | 57 |
| | | Grazing | 368.3 | 52 |
| Ag-Au | | Normal | 368.2 | 65 |
| | | Grazing | 368.2 | 64 |
| Au@Ag | | Normal | 368.4 | 65 |
| | | Grazing | 368.2 | 69 |

In the case of the Ag@Au system, the amount of silver detected decreased as the extraction angle of the emitted signal became more grazing, indicating that the silver was mainly located in the core of the BNPs. For Au@Ag, the opposite trend was observed, the change in angle leading to an increase in the silver amount, indicating that the silver is more likely to be located on the BNP shell. Finally, similar atomic percentages were obtained for the Ag-Au alloy, confirming its formation (Table 4).

Photo-induced synthesis of double-shelled system Ag@Au@Ag:

It is important to emphasize that the photoinduced approach allows synthesis of increasingly complex nanoobjects. In this case, the residual AgCl observed by EXAFS in the Ag@Au formulation was used for the formation of a second shell by only increasing the UV exposure time to 45 mins. The absorption spectra (Figure 7a) obtained by UV-Vis spectroscopy show a blue shift of the resonance peak from 441 to 427 nm and an increase in peak intensity, which seems to indicate the growth of a second silver shell surrounding the existing gold shell. In parallel, it was observed that the gold resonance peak becomes progressively less visible with increasing exposure time, due to the growth of a silver layer around the gold layer, masking its signal, as previously observed for the growth of Au@Ag BNPs. The colour of the sample thus changes from red (the colour of the Ag@Au system) to orange, which would be the signature of an Ag@Au@Ag system (photos in Figure 7a).

TEM micrographs of the same sample also show a slight increase in the average size of the NPs from 4.4 nm to 4.6 nm (Figure 7b), which could be correlated with the growth of a second 0.2 nm thick shell.

Finally, the comparison of the Fourier transforms of the EXAFS oscillations (Figure 7c) recorded at the K-Ag edge between the Ag@Au 45 min sample and that of a reference silver foil indicates that the environment around the silver atoms is close to that of an Ag(0) metal. The absence of peaks in the Fourier transforms due to the presence of AgCl and AgNO₃ confirms that the silver in this formulation was completely reduced after 45 mins under UV.

The J_{Ag} and J_{Au} calculations of both silver and gold coordination numbers derived from the combined simulation of the EXAFS signals recorded at the two thresholds, gives 46 and 30 % respectively. The simulations made for these spectra are shown in the SI (Figure S2). Although

Hwang's structural model is not necessarily suitable for studying an Ag@Au@Ag double shell system, these values are very close to those obtained for an Au@Ag core-shell system. It seems as though an Ag@Au@Ag system was obtained with a small silver core surrounded by a thick layer of gold, which in turn, was covered by a thin silver shell.

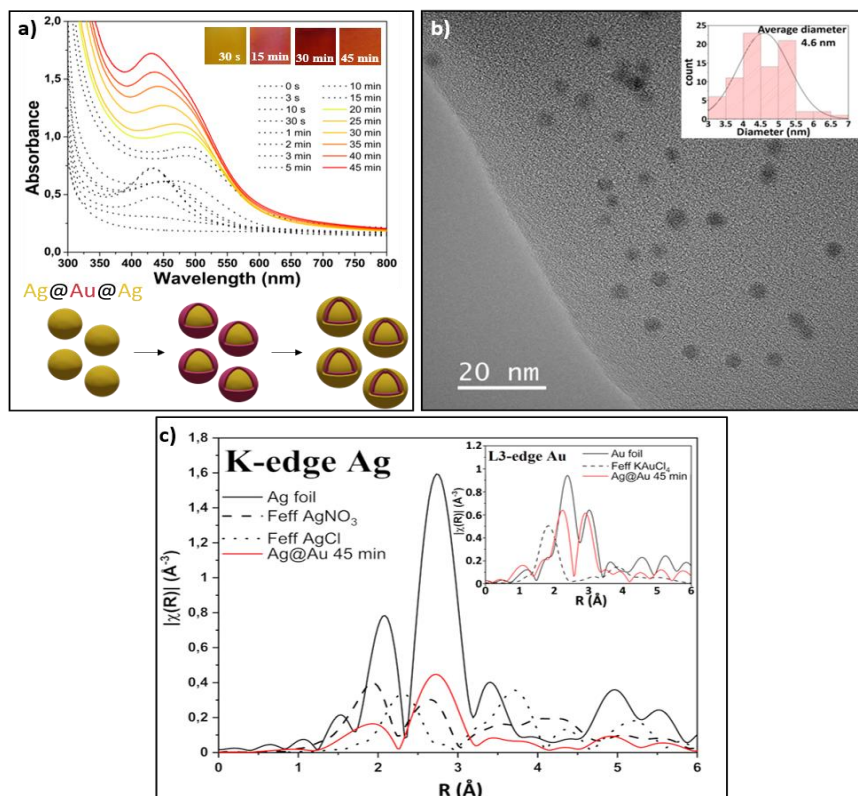


Figure 7. a) UV-visible spectra over increased exposure time, inserts are pictures of the sample at 30 s, 15 mins, 30 mins and 45 mins. b) TEM micrograph with in insert the size histogram of NPs. c) EXAFS data for the K-edge Ag with an insert of the EXAFS data for L3-edge Au.

Conclusion:

An efficient method to create bimetallic plasmon-active polymer coatings in a single step by using a simple UV source has been developed. This process involves the formation of Ag and Au BNPs and their stabilisation within a photopolymerisable PEGDA matrix. Moreover, it was

possible to tune the optical properties of the BNPs by carefully controlling the order of the metal precursor reductions into the photosensitive formulation. This control allows the generation of different types of BNPs systems, including core-shell (Ag@Au or Au@Ag) and alloy (Ag-Au) structures. The particles are spherical and well dispersed in the polymer with an average diameter of 4-6 nm. In the first Ag@Au system, the kinetic study carried out by UV-Vis, TEM and EXAFS shows a growth starting with the silver core formation followed by the gold shell. However, since the Ag⁺ was partially reduced in the first step, the synthesis of these particular BNPs can be pushed further to form a more complex structure and add another shell, resulting in a double shelled Ag@Au@Ag system. Moreover, core-shells Au@Ag with a gold core were obtained directly by a second synthesis protocol where, gold was reduced before silver. Finally, on the alloy BNPs, the simultaneous growth of both nanoparticles results in an alloy with 54 % silver according to the LSPR. The monitoring of the BNP growth kinetics at different steps was possible using UV-Vis spectroscopy, EXAFS and TEM (EDS/STEM-HAADF), showing that can be easy to tune the photoinduced reactions and form the desired BNPs system.

Regardless BNPs nature (Ag@Au, Au@Ag and Ag-Au), all systems, exhibited plasmon resonance activity demonstrating their potential in tuning the optical properties of functional coatings, with a wide range of possible applications.

The new plasmonic coating can easily tune the LSPR bands, which is expected to be applied to SERS and other applications.

Supporting Information:

Additional methods for the fits of UV-vis spectra and EXAFS, description of the structural model used with the EXAFS, additional HRTEM and STEM-HAADF imaging and experimental details for UV-vis monitoring of NPs synthesis and display of XPS spectra (.docx)

AUTHOR INFORMATION

Corresponding Author:

* lavinia.balan@cnrs-orleans.fr (ORCID 0000-0003-0144-401X)

Author Contributions

The manuscript was written through contributions of all authors. All authors have given approval to the final version of the manuscript.

Funding Sources

The authors express their thanks to the Agence Nationale de la Recherche (ANR) for their financial support under contract ANR-21-CE06-0046.

ACKNOWLEDGMENT

This project has benefited from the expertise and the facilities of the Platform MACLE-CVL which was co-funded by the European Union and Centre-Val de Loire Region (FEDER)

The EXAFS beamtime was provided by the SOLEIL synchrotron (Gif-sur-Yvette, France) as part of the project 20220964.

REFERENCES

- [1] Elemike E. E.; Onwudiwe D. C.; Nundkumar N.; Singh M.; Iyekowa O. Green synthesis of Ag, Au and Ag-Au bimetallic nanoparticles using *Stigmaphyllon ovatum* leaf extract and their in vitro anticancer potential. *Materials Letters*, **2019**, 243, 148-152. DOI: 10.1016/j.matlet.2019.02.049
- [2] Nalawade P.; Mukherjee P.; Kapoor S. Triethylamine induced synthesis of silver and bimetallic (Ag/Au) nanoparticles in glycerol and their antibacterial study, *Journal of Nanostructure in Chemistry*, **2014**, 4, 113. DOI: 10.1007/s40097-014-0113-2
- [3] Holden M. S.; Black J.; Lewis A.; Boutrin M. C.; Walemba E.; Sabir T. S.; Boskovic D. S.; Wilson A.; Fletcher H. M.; Perry C. C.; Antibacterial activity of partially oxidized Ag/Au nanoparticles against the oral pathogen *Porphyromonas gingivalis* W83, *Journal of Nanomaterials*, **2016**, 2016, 1–11. DOI: 5.223462656e-10
- [4] de Alwis Weerasekera H.; Silvero M. J.; da Silva D. R. C.; Scaiano J. C. A database on the stability of silver and gold nanostructures for applications in biology and biomolecular sciences, *Biomaterials Science*, **2017**, 5, 89-97. DOI: 10.1039/c6bm00629a
- [5] Ferrer D. A.; Diaz-Torres L. A.; Wu S.; Jose-Yacaman M. Crystalline order of silver-gold nanocatalysts with hollow-core and alloyed-shell, *Catalysis Today*, **2009**, 147, 211-216. DOI: 10.1016/j.cattod.2009.02.047
- [6] Emam H. E.; El-Zawahry M. M.; Ahmed H. B. One-pot fabrication of AgNPs, AuNPs and Ag-Au nano-alloy using cellulosic solid support for catalytic reduction application, *Carbohydrate Polymers*, **2017**, 166, 1-13. DOI: 10.1016/j.carbpol.2017.02.091

[7] Kumari M. M.; Jacob J.; Philip D. Green synthesis and applications of Au-Ag bimetallic nanoparticles, *Spectrochimica Acta - Part A: Molecular and Biomolecular Spectroscopy*, **2015**, 137, 185-192. DOI: 10.1016/j.saa.2014.08.079

[8] Leishangthem D.; Yumkhaibam M. A. K.; Henam P. S.; Nagarajan S. An insight into the effect of composition for enhance catalytic performance of biogenic Au/Ag bimetallic nanoparticles, *Journal of Physical Organic Chemistry*, **2018**, 31, 10.1002/poc.3815. DOI: 10.1002/poc.3815

[9] Xiang F.; Gan W. Factors influencing the preparation of silver-coated glass frit with polyvinyl-pyrrolidone, *Materials Research Express*, **2018**, 5, 015008. DOI: 10.1088/2053-1591/aa9fd4

[10] Zhang L.; Wang Z. S. Gold nanoparticles as an ultrathin scattering layer for efficient dye-sensitized solar cells, *Journal of Materials Chemistry C*, **2016**, 4, 3614-3620. DOI: 10.1039/c6tc00592f

[11] Loiseau A.; Asila V.; Boitel-Aullen G.; Lam M.; Salmain M.; Boujday S. Silver-based plasmonic nanoparticles for and their use in biosensing, *Biosensors*, **2019**, 9, 78. DOI: 10.3390/bios9020078

[12] Sun L.; Li Q.; Tang W.; Di J.; Wu Y. The use of gold-silver core-shell nanorods self-assembled on a glass substrate can substantially improve the performance of plasmonic affinity biosensors, *Microchimica Acta*, **2014**, 181, 1991-1997. DOI: 10.1007/s00604-014-1285-7

[13] Dong P.; Wu Y.; Guo W.; Di J. Plasmonic Biosensor Based on Triangular Au/Ag and Au/Ag/Au Core/Shell Nanoprisms onto Indium Tin Oxide Glass, *Plasmonics*, **2013**, 8, 1577-1583. DOI: 10.1007/s11468-013-9574-2

[14] Dong P.; Lin Y.; Deng J.; Di J. Ultrathin gold-shell coated silver nanoparticles onto a glass platform for improvement of plasmonic sensors, *ACS Applied Materials and Interfaces*, **2013**, 5, 2392-2399. DOI: 10.1021/am4004254

[15] Guselnikova O.; Lim H.; Kim H.; Kim S. H.; Gorbunova A.; Eguchi M.; Postnikov P.; Nakanishi T.; Asahi T.; Na J.; Yamauchi Y. New Trends in Nanoarchitected SERS Substrates: Nanospaces, 2D Materials, and Organic Heterostructures, *Small*, **2022**, 18. DOI: 10.1002/sml.202107182

[16] Lim H.; Nagaura T.; Kim M.; Kani K.; Kim J.; Bando Y.; Alshehri S. M.; Ahamad T.; You J.; Na J.; Yamauchi Y. Electrochemical preparation system for unique mesoporous hemisphere gold nanoparticles using block copolymer micelles, *RSC Advances*, **2020**, 10, 8309–8313. DOI: 10.1039/d0ra01072c

[17] Andreazza P.; Pierron-Bohnes V.; Tournus F.; Andreazza-Vignolle C.; Dupuis V. Structure and order in CoPt-type nanoalloys: From thin films to supported clusters, *Surface Science Reports*, **2015**, 70, 188-258. DOI: 10.1016/j.surfrep.2015.02.002

[18] Murugadoss A.; Kai N.; Sakurai H. Synthesis of bimetallic gold-silver alloy nanoclusters by simple mortar grinding, *Nanoscale*, 2012, 4, 4, 1280-1282, DOI: 10.1039/c2nr11727d

[19] Gao C.; Hu Y.; Wang M.; Chi M.; Y. Yin, Fully alloyed Ag/Au nanospheres: Combining the plasmonic property of Ag with the stability of Au, *Journal of the American Chemical Society*, **2014**, 136, 7474-7479. DOI: 10.1021/ja502890c

[20] Jara N.; Milán N. S.; Rahman A.; Mouheb L.; Boffito D. C.; Jeffryes C.; Dahoumane S. A.; Photochemical synthesis of gold and silver nanoparticles-a review, *Molecules*, **2021**, 26, 4585. DOI: 10.3390/molecules26154585

[21] Ristig S.; Prymak O.; Loza K.; Gocyla M.; Meyer-Zaika W.; Heggen M.; Raabe D.; Epple M. Nanostructure of wet-chemically prepared, polymer-stabilized silver-gold nanoalloys (6 nm) over the entire composition range, *Journal of Materials Chemistry B*, **2015**, 3, 4654-4662. DOI: 10.1039/c5tb00644a

[22] Pal A.; Shah S.; Kulkarni V.; Murthy R. S. R.; Devi S. Template free synthesis of silver-gold alloy nanoparticles and cellular uptake of gold nanoparticles in Chinese Hamster Ovary cell, *Materials Chemistry and Physics*, **2009**, 113, 1, 276-282. DOI: 10.1016/j.matchemphys.2008.07.072

[23] Pal A.; Shah S.; Devi S. Preparation of silver, gold and silver-gold bimetallic nanoparticles in w/o microemulsion containing TritonX-100, *Colloids and Surfaces A: Physicochemical and Engineering Aspects*, **2007**, 302, 483-487. DOI: 10.1016/j.colsurfa.2007.03.032

[24] ur-Rahman L.; Shah A.; Khan S. B.; Asiri A. M.; Hussain H.; Han C.; Qureshi R.; Ashiq M. N.; Zia M. A.; Ishaq M.; Kraatz H.-B. Synthesis, characterization, and application of Au-Ag alloy nanoparticles for the sensing of an environmental toxin, pyrene, *Journal of Applied Electrochemistry*, **2015**, 45, 463-472. DOI: 10.1007/s10800-015-0807-2

[25] Pal A.; Shah S.; Devi S. Synthesis of Au, Ag and Au-Ag alloy nanoparticles in aqueous polymer solution, *Colloids and Surfaces A: Physicochemical and Engineering Aspects*, **2007**, 302, 51-57. DOI: 10.1016/j.colsurfa.2007.01.054

[26] Kuppusamy P.; Ilavenil S.; Srigopalram S.; Kim D. H.; Govindan N.; Maniam G. P.; Yusoff M. M.; Choi K. C. Synthesis of Bimetallic Nanoparticles (Au–Ag Alloy) Using *Commelina nudiflora* L. Plant Extract and Study its on Oral Pathogenic Bacteria, *Journal of Inorganic and Organometallic Polymers and Materials*, **2017**, 27, 562-568. DOI: 10.1007/s10904-017-0498-8

[27] Ghodselahi T.; Arsalani S.; Neishaboorynejad T. Synthesis and biosensor application of Ag@Au bimetallic nanoparticles based on localized surface plasmon resonance, *Applied Surface Science*, **2014**, 301, 230-234. DOI: 10.1016/j.apsusc.2014.02.050

[28] Wang P.; Wei S.; Tong L.; He X.; Bai Y.; Jia K.; Liu X. An immunosensor based on Au-Ag bimetallic NPs patterned on a thermal resistant flexible polymer substrate for in-vitro protein detection, *Polymers*, **2019**, 11, 1257. DOI: 10.3390/polym11081257

[29] Corpuz R. D.; Ishida Y.; Nguyen M. T.; Yonezawa T. Synthesis of Positively Charged Photoluminescent Bimetallic Au-Ag Nanoclusters by Double-Target Sputtering Method on a Biocompatible Polymer Matrix, *Langmuir*, **2017**, 33, 9144-9150. DOI: 10.1021/acs.langmuir.7b02011

[30] Fahes A.; Naciri A. E.; Shoker M. B.; Akil S. Self-assembly-based integration of Ag@Au oligomers and core/shell nanoparticles on polymer chips for efficient sensing devices, *Soft Matter*, **2023**, 19, 321–330. DOI: 10.1039/d2sm00769j

[31] Shin Y.; Bae I. T.; Arey B. W.; Exarhos G. J. Facile stabilization of gold-silver alloy nanoparticles on cellulose nanocrystal, *Journal of Physical Chemistry C*, **2008**, 112, 4844-4848. DOI: 10.1021/jp710767w

[32] Ahmed M. K.; Zayed M. A.; El-dek S. I.; Hady M. A.; Sherbiny D. H. E.; Uskoković V. Nanofibrous ϵ -polycaprolactone scaffolds containing Ag-doped magnetite nanoparticles: Physicochemical characterization and biological testing for wound dressing applications in vitro and in vivo, *Bioactive Materials*, **2021**, 6, 2070-2088. DOI: 10.1016/j.bioactmat.2020.12.026

[33] Zouari H. B.; Dabert M.; Asia L.; Wah-Chung P. W.; Baba M.; Balan L.; Israëli Y. Influence of in situ photo-induced silver nanoparticles on the ageing of acrylate materials, *Journal of Photochemistry and Photobiology A: Chemistry*, **2021**, 408, 113112. DOI: 10.1016/j.jphotochem.2020.113112

[34] Zaier M.; Vidal L.; Hajjar-Garreau S.; Balan L. Generating highly reflective and conductive metal layers through a light-assisted synthesis and assembling of silver nanoparticles in a polymer matrix, *Scientific Reports*, **2017**, 7, 113112. DOI: 10.1038/s41598-017-12617-8

[35] Plé J.; Dabert M.; Lecoq H.; Hellé S.; Ploux L.; Balan L. Antimicrobial and mechanical properties of functionalized textile by nanoarchitected photoinduced Ag@polymer coating, *Beilstein Journal of Nanotechnology*, **2023**, 14, 95-109. DOI: 10.3762/bjnano.14.11

[36] Schejn A.; Ott M.; Dabert M.; Vidal L.; Balan L. Photo-induced design of reflective metallized gold@polymer coatings with tuned architecture, *Materials and Design*, **2018**, 160, 74-83. DOI: 10.1016/j.matdes.2018.08.051

[37] Ravel B.; Newville M. ATHENA, ARTEMIS, HEPHAESTUS: data analysis for X-ray absorption spectroscopy using IFEFFIT, *Journal of Synchrotron Radiation*, **2005**, 12, 537–541. DOI: 10.1107/s0909049505012719

[38] Hwang B.-J.; Sarma L. S.; Chen J.-M.; Chen C.-H.; Shih S.-C.; Wang G.-R.; Liu D.-G.; Lee J.-F.; Tang M.-T. Structural Models and Atomic Distribution of Bimetallic Nanoparticles as Investigated by X-ray Absorption Spectroscopy, *Journal of the American Chemical Society*, **2005**, 127, 11140–11145. DOI: 10.1021/ja0526618

[39] Joo J. H.; Kim B.-H.; Lee J.-S. Synthesis of Gold Nanoparticle-Embedded Silver Cubic Mesh Nanostructures Using AgCl Nanocubes for Plasmonic Photocatalysis, *Small*, **2017**, 13, 1701751. DOI: 10.1002/smll.201701751

[40] Bard A. J.; Parsons R.; Jordan J. Standard Potentials in Aqueous Solution, **2017**. DOI: 10.1201/9780203738764

[41] Vanýsek P. Electrochemical Series, ASM International, **2005**, 665–671. DOI: 10.31399/asm.hb.v13b.a0006542

[42] Zhao H.; Wang F.; Ning Y.; Zhao B.; Yin F.; Lai Y.; Zheng J.; Hu X.; Fan T.; Tang J.; Zhang D.; Hu K. Green "planting" nanostructured single crystal silver, *Scientific Reports*, **2013**, 3, 1511. DOI: 10.1038/srep01511

[43] Rao P. S.; Hayon E. Redox potentials of free radicals. I. Simple organic radicals, *Journal of the American Chemical Society*, **1974**, 96, 1287–1294. DOI: 10.1021/ja00812a004

[44] Lin Z. W.; Qi S. L.; Wu D. Z. Formation of double-surface-silvered polyimide films via a direct ion-exchange self-metallization technique: The case of BPADA/ODA and $[\text{Ag}(\text{NH}_3)_2]^+$, *Journal of Applied Polymer Science*, **2012**, 125, 3552-3559. DOI: 10.1002/app.36240

[45] Gorup L. F.; Longo E.; Leite E. R.; Camargo E. R. Moderating effect of ammonia on particle growth and stability of quasi-monodisperse silver nanoparticles synthesized by the Turkevich method, *Journal of Colloid and Interface Science*, **2011**, 360, 355–358. DOI: 10.1016/j.jcis.2011.04.099

[46] Boufi S.; Vilar M. R.; Ferraria A. M.; do Rego A. M. B. In situ photochemical generation of silver and gold nanoparticles on chitosan, *Colloids and Surfaces A: Physicochemical and Engineering Aspects*, **2013**, 439, 151-158. DOI: 10.1016/j.colsurfa.2012.12.036

[47] Gonzalez C. M.; Martin B.; Betancourt T. Photochemical synthesis of bimetallic and anisotropic Au-containing nanoparticles using a one-step protocol, *Journal of Materials Chemistry A*, **2014**, 2, 17574-17585. DOI: 10.1039/c4ta03974b

[48] Gonzalez C. M.; Liu Y.; Scaiano J. C. Photochemical strategies for the facile synthesis of gold-silver alloy and core-shell bimetallic nanoparticles, *Journal of Physical Chemistry C*, **2009**, 113, 11861-11867. DOI: 10.1021/jp902061v

[49] Shin K. S.; Kim J. H.; Kim I. H.; Kim K., Novel fabrication and catalytic application of poly(ethylenimine)- stabilized gold-silver alloy nanoparticles, *Journal of Nanoparticle Research*, **2012**, 14, 735. DOI: 10.1007/s11051-012-0735-6

[50] Cortie M. B.; McDonagh A. M. Synthesis and Optical Properties of Hybrid and Alloy Plasmonic Nanoparticles, *Chemical Reviews*, **2011**, 111, 3713–3735. DOI: 10.1021/cr1002529

[51] Eremenko A. M.; Smirnov N. P.; Mukhal I. P.; Yashan H. R. Silver and gold nanoparticles in silica matrices: synthesis, properties, and application, *Theoretical and Experimental Chemistry*, **2010**, 46, 65–88. DOI: 10.1007/s11237-010-9122-5

[52] Pande S.; Ghosh S. K.; Praharaj S.; Panigrahi S.; Basu S.; Jana S.; Pal A.; Tsukuda T.; Pal T. Synthesis of normal and inverted gold-silver core-shell architectures in β -cyclodextrin and their applications in SERS, *Journal of Physical Chemistry C*, **2007**, 111, 10806-10813. DOI: 10.1021/jp0702393

[53] Li Z. Y.; Yuan J.; Chen Y.; Palmer R. E.; Wilcoxon J. P. Direct imaging of core-shell structure in silver-gold bimetallic nanoparticles, *Applied Physics Letters*, **2005**, 87, 243103. DOI: 10.1063/1.2139851

[54] Ankudinov A. L.; Ravel B.; Rehr J. J.; Conradson S. D. Real-space multiple-scattering calculation and interpretation of x-ray-absorption near-edge structure, *Physical Review B*, **1998**, 58, 7565–7576. DOI: 10.1103/physrevb.58.7565

[55] Godfrey I. J.; Dent A. J.; Parkin I. P. Maenosono S.; Sankar G. Structure of Gold–Silver Nanoparticles, *The Journal of Physical Chemistry C*, **2017**, 121, 1957–1963. DOI: 10.1021/acs.jpcc.6b11186

[56] Knecht M. R.; Weir M. G.; Frenkel A. I.; Crooks R. M. Structural Rearrangement of Bimetallic Alloy PdAu Nanoparticles within Dendrimer Templates to Yield Core/Shell Configurations, *Chemistry of Materials*, **2007**, 20, 1019–1028. DOI: 10.1021/cm0717817.